Applied Surface Science 515 (2020) 145972

Contents lists available at ScienceDirect

Applied Surface Science

journal homepage: www.elsevier.com/locate/apsusc

Full Length Article

Role of anionic vacancy for active hydrogen evolution in WTe_2

Hagyeong Kwon[a,1], Byungdo Ji[b,1], Dongyeon Bae[a], Jun-Ho Lee[c], Hee Jung Park (Dr.)[d], Do Hyun Kim[b], Young-Min Kim[b,e], Young-Woo Son[c], Heejun Yang[b,*], Suyeon Cho[a,*]

[a] Division of Chemical Engineering and Materials Science, Ewha Womans University, Seoul 03760, Republic of Korea
[b] Department of Energy Science, Sungkyunkwan University, Suwon 16419, Republic of Korea
[c] Korea Institute for Advanced Study, Seoul 02455, Republic of Korea
[d] Western Seoul Center, Korea Basic Science Institute, Seoul, 03759, Republic of Korea
[e] IBS Center for Integrated Nanostructure Physics (CINAP), Institute for Basic Science, Sungkyunkwan University, Suwon 16419, Republic of Korea

ARTICLE INFO

Keywords:
Hydrogen evolution reaction
Transition metal dichalcogenides
WTe_2
Anion vacancy
Work function

ABSTRACT

Transition metal dichalcogenides (TMDs) have been investigated for use in a hydrogen evolution reaction (HER), mostly in the form of nano-sized flakes, due to the abundant active site formation by nanostructuring, surface functionalization, and phase engineering. However, the physical origin of the active HER on TMDs remains to be clarified. Here, we investigate the role of anion vacancies for the HER on the basal plane of single-crystalline tungsten dichalcogenide (WTe_2), a group 6 metallic TMD. The WTe_2 with a small amount of anionic (Te) vacancies shows an improved overpotential from –0.707 to –0.568 V and a constant Tafel slope of 154 mV/dec in the HER. Photoemission spectroscopy, combined with first-principle calculations, reveals that the work function of WTe_2 is decreased by the anionic Te vacancies, which improves the bulk conductivity and the overpotential in the HER with the material. Moreover, the enlarged electrochemical active surface area with a large number of Te vacancies in the WTe_2 critically improves the HER performance with decreases in the overpotential and the Tafel slope, –0.119 V and 79 mV/dec, respectively. Our results show that the modulation of work function and surface morphology is a promising way to improve the HER in TMDs.

1. Introduction

The use of fossil fuel inevitably produces carbon dioxide, which results in air pollution as well as global warming. Accordingly, extensive efforts have been made to develop alternative clean energy sources [1,2]. Among possible solutions, hydrogen has received considerable attention as an ideal energy source because of its large energy density and clean final product, water [3,4]. While the major industrial method to produce hydrogen—steam reforming of methane—still uses considerable fossil fuels and emits carbon dioxide, hydrogen generation based on electrolysis has been suggested as a sustainable, clean, and renewable way for the mass production of hydrogen. For this purpose, it is important to develop efficient electrochemical catalysts based on earth-abundant elements that can replace expensive noble metal-based electrochemical catalysts.

Layered transition metal dichalcogenides (TMDs), particularly semiconducting TMDs, have been extensively studied because of their low cost and abundant catalytic active sites [5–9]. Jaramillo et al. reported that hexagonal MoS_2, a group 6 TMD semiconductor, exhibits a highly catalytic activity in the hydrogen evolution reaction (HER); the conductive edges and defects were suggested for the origin of the active HER [10]. To further enhance the catalytic activity of semiconducting TMDs, hybridization with other conducting materials and alkali–ion intercalation have been tried; an increased electron transfer rate via phase transition improves the electrochemical catalytic reaction, the HER [11–14]. Phase engineering and nanostructuring for hybrid electrochemical catalysts with semiconducting TMDs have shown impressive catalytic performances due to their abundant conducting active sites, such as increased densities of edges or defects [15–17]. However, the increased defect and edge densities in the TMDs make it difficult to clarify the origin of the improved HER at the atomic scale in the materials.

Based on the polymorphism in TMDs, structural phase engineering has been extensively studied for the HER with group 6 TMDs. Phase

* Corresponding authors.
E-mail addresses: khk960621@gmail.com (H. Kwon), owenba@naver.com (B. Ji), ehddus0904@gmail.com (D. Bae), junholee@lbl.gov (J.-H. Lee), hjpark8659@kbsi.re.kr (H.J. Park), kkkddd2002@naver.com (D.H. Kim), youngmk@skku.edu (Y.-M. Kim), hand@kias.re.kr (Y.-W. Son), h.yang@skku.edu (H. Yang), s.cho@ewha.ac.kr (S. Cho).
[1] These authors contributed equally to this work.

https://doi.org/10.1016/j.apsusc.2020.145972
Received 16 November 2019; Received in revised form 10 February 2020; Accepted 2 March 2020
Available online 03 March 2020

engineering has demonstrated enhanced catalytic performances by providing catalytically-active metallic (1T or 1T') areas to the semiconducting hexagonal (2H) TMDs [18–20]. For example, metallic trigonal (1T) MoS_2 inhomogeneously fabricated by alkali–ion intercalation exhibits active HER performances; however, the metallic phase possesses poor chemical stability due to its metastable nature.

Among the group 6 TMDs, $MoTe_2$ and WTe_2 have a thermodynamically-stable metallic phase (distorted octahedral or 1T') that exhibits unique physical and electrochemical properties [21–23]. In particular, unlike $MoTe_2$, WTe_2 has a single metallic phase without a semiconducting phase. Both the metallic $MoTe_2$ and WTe_2 possess lattice distortion implying charge density wave (CDW) states in the materials. Seok et al. reported that the metallic basal plane (1T') of $MoTe_2$ serves as an active area with a uniquely localized electron density [24]. The calculated Gibbs free energy for hydrogen adsorption suggests that the basal plane of metallic TMDs can be catalytically active with a high turn-over frequency similar to that of a platinum catalyst [25–29].

In this study, we improved the catalytic activity of WTe_2 single crystals by introducing Te deficiencies at the surface of WTe_2. Thermal reduction in a vacuum and electrochemical reduction in an acidic solution were used for the surface modification. The morphology and chemical state changes of the WTe_2 surface were studied by atomic force microscopy (AFM), scanning electron microscopy (SEM), and *in-situ* photoelectron spectroscopy with X-ray and ultraviolet (UV) light sources (XPS and UPS). Quantitative analysis using an electron probe microanalyzer (EPMA), energy dispersive X-ray analyzer (EDX), and XPS demonstrated that the ratio of Te and W atoms decreased dramatically after the surface treatment. *In-situ* UPS measurements, combined with first-principles calculations, demonstrated a decrease in the work function in Te-deficient WTe_2, which contributed partially to the enhancement of the bulk electrical conductivity in metallic WTe_2. We found that the explosive increase of the surface area via Te deficiency-driven surface modification played a crucial role for the improved HER in metallic TMDs. Thus, our systematic study clarified the role of anionic chalcogen vacancies in the HER with metallic TMDs.

2. Experimental

Metallic WTe_2 single crystals were grown by a flux method that was similar to our previous report [30]. The detailed synthetic conditions are described in the supporting materials. The crystallographic properties of the WTe_2 single crystal were investigated by an X-ray diffractometer (Rigaku, SmartLab) with Cu Kα radiation (λ = 1.54059 Å) in the Bragg–Brentano geometry.

To study the role of Te vacancies in the HER, Te vacancies at the surface of a WTe_2 single crystal were created by two different methods, vacuum-annealing and electrochemical reduction. For the vacuum-annealing, WTe_2 single crystals were annealed at 373 K for 1 h in a tube furnace with a vacuum level of 10^{-2} Torr. For the electrochemical reduction, multiple cyclic voltammetry (CV) was conducted between a WTe_2 electrode and a glassy carbon electrode in a voltage range between 0 and –1.2 V vs. RHE with a scan rate of 100 mV/s.

The HER experiments were performed using a three-electrode cell employing 200 mL of a 0.5 M sulfuric acid (H_2SO_4) electrolyte solution at room temperature. A silver/silver chloride electrode (Ag/AgCl, Qrins, Korea), a glassy carbon electrode (Qrins, Korea), and the WTe_2 single crystal were used as the reference, counter, and working electrodes, respectively (Fig. S1). Linear sweep voltammetry (LSV) was conducted at a scan rate of 5 mV/s using a potentiostat (VMP3 from Bio Logic, France). The same experimental setup was used for the electrochemical active surface area (ECSA) analysis with a voltage range from 0.035 to 0.16 V vs. RHE and sweep rates of 20, 50, 80,100, and 200 mV/s.

Atom-resolved high-angle annular dark-field (HAADF) scanning transmission electron microscopy (STEM) imaging was performed with a probe-corrected transmission electron microscope (TEM) operated at 200 keV (JEM-ARM200F, JEOL, Japan). Scanning tunneling microscopy (STM) images were obtained using Omicron STM (Germany) at room temperature in an ultra-high-vacuum (UHV) chamber (base pressure: ~1×10^{-10} Torr). For the chemical analysis of the WTe_2 catalyst surface, we conducted XPS and UPS in an ultra-high-vacuum (UHV) chamber (base pressure: ~1×10^{-10} Torr) with photon energy of 1486 eV and 21.218 eV, respectively. The electron analyzers were an ESCALAB 250Xi XPS Microprobe (Thermo-Scientific) for XPS and Scienta R4000 spectromicroscopy (Scienta) for UPS. The roughness analysis with *in-situ* vacuum annealing were performed by an atomic force microscopic (AFM) system (SEIKO E-sweep AFM with a base pressure of ~1×10^{-8} Torr). The surface morphologies together with quantitative analysis were checked by a field-emission scanning electron microscopy (FE-SEM) system (Hitachi SU8220 FE-SEM with a base pressure of ~1×10^{-7} Torr) at the Western Seoul Center, Korea Basic Science Institute.

First-principles calculations were conducted using a Quantum ESPRESSO package [31]. We used norm-conserving pseudopotentials for W, Te, and H atoms, a plane wave energy cutoff of 80 ryd, a PBE exchange-correlation functional [32], and equilibrium lattice parameters of a = 6.36 Å and b = 3.53 Å to simulate the orthorhombic WTe_2 structure.

3. Results and discussions

The WTe_2 layers composed of distorted octahedrons (Fig. 1a) and distorted octahedral structural units with two different Te sites, α and β, that resulted in atomic distortion at the WTe_2 surface are shown in the STM image (Fig. 1b). High-resolution scanning transmission electron microscopy (STEM) imaging shows that the WTe_2 layers were separated by a van der Waals gap of roughly 4 Å along the c-axis (Fig. 1c). A lattice distortion of Te atoms was visible along the a-axis, which indicated a charge density wave (CDW) on the WTe_2 similar to that reported for $MoTe_2$ [24].

The bulk properties of the vacuum-annealed WTe_2 single crystal were investigated using XRD and Raman spectroscopy before and after

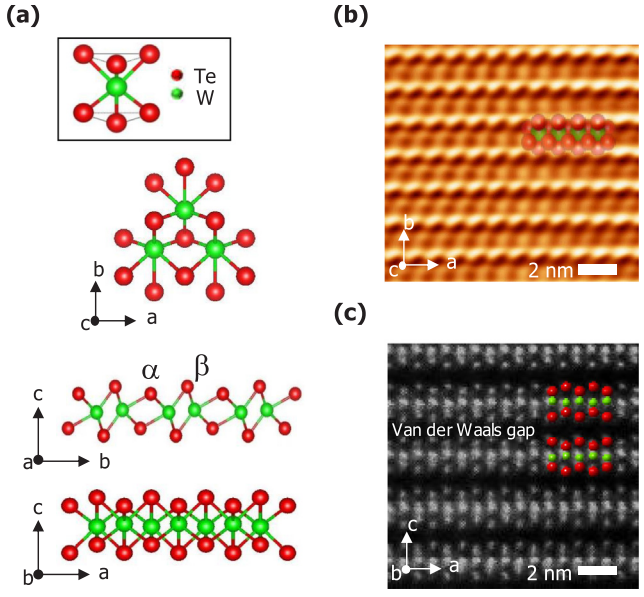

Fig. 1. (a) Schematic illustration of WTe_2 layer with the octahedral structural unit of WTe_2 (inset). Structural distortion due to the charge density wave results in nonuniform atomic distribution (top view) and a bucked structure (side view) with different Te sites α and β. (b) High-resolution atomic STM image projected in the (0 0 1) direction clearly shows the nonuniform atomic arrangement. (c) HAADF-STEM image projected in the (0 1 0) direction clearly shows the van der Waals gaps between WTe_2 layers.

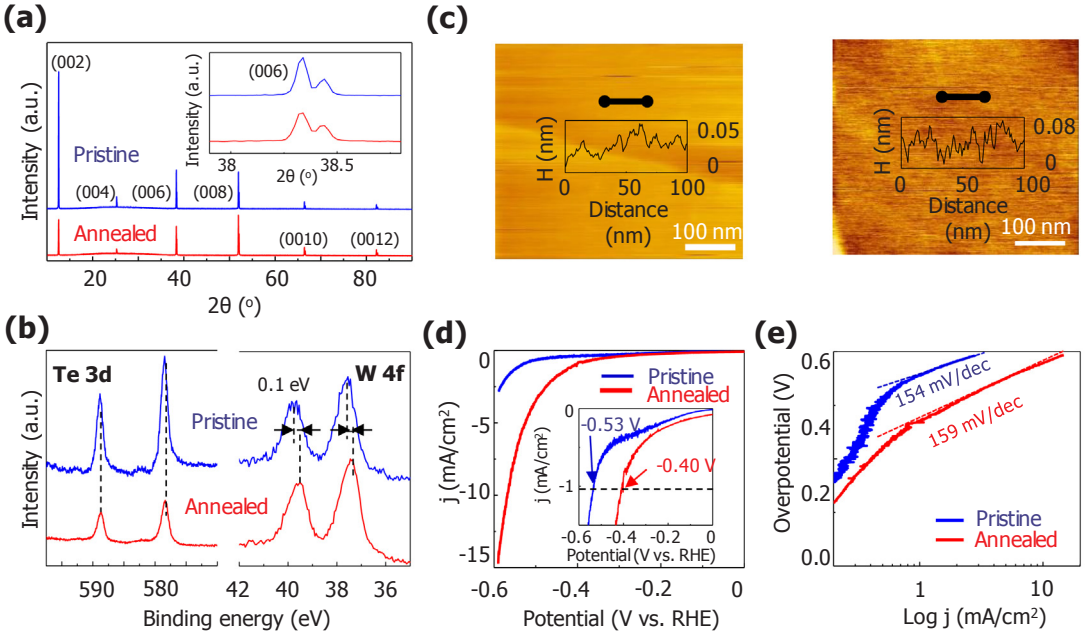

Fig. 2. (a) X-ray diffraction patterns of pristine (blue) and annealed (red) WTe_2 single crystal. (b) X-ray photoemission spectra of core levels, W *4f*, and Te *3d* obtained for pristine (blue) and annealed (red) WTe_2 single crystals. (c) AFM images of exfoliated WTe_2 microsized single crystal before and after *in-situ* vacuum-annealing process. Line profiles across the surface (black lines) were acquired to estimate the surface roughness of pristine and annealed WTe_2. (d) Linear sweep voltammetry polarization curves acquired for pristine and annealed WTe_2 single crystals. Overpotentials were measured at the current density of 1 mA/cm^2 (inset). (e) Tafel plots of pristine and annealed WTe_2 single crystals. The inset shows the optical image of the tested WTe_2 single crystal. (For interpretation of the references to colour in this figure legend, the reader is referred to the web version of this article.)

vacuum-annealing of single-crystalline WTe_2. Fig. 2a shows the diffraction peaks of the pristine and annealed WTe_2 single crystal. The diffraction peaks corresponding to (00n) planes did not show any significant angle shift (inset of Fig. 2a) and no other structural phases such as segregated metallic phases (W or Te) or nonstoichiometric phases were found in the diffraction patterns. Raman spectra (Fig. S2) obtained for the pristine and annealed WTe_2 single crystal also showed no significant changes in the Raman-active peaks at 118 cm^{-1} (A_1^3), 134 cm^{-1} (A_1^5), 164 cm^{-1} (A_1^7), and 212 cm^{-1} (A_1^9), as reported in a previous study [33].

To study the surface chemistry of Te-deficient WTe_2, surface-sensitive photoemission spectroscopy was performed before and after the *in-situ* vacuum-annealing at T = 373 K for 30 min with a vacuum of 1×10^{-8} Torr. Fig. 2b shows the core level spectra of W *4f* and Te *3d* of WTe_2. No other secondary phases were found before and after the annealing process. As seen in Fig. 2b, the W *4f* peak in the Te-deficient WTe_2 surface shifted by 0.10 eV, while the Te *3d* peaks remained almost unchanged after the Te deficiency was created. Since W atoms are surrounded by Te atoms in the octahedral form, the Te deficiency influenced the chemical state of W *4f* but hardly affected the chemical state of Te *3d*. The relative ratio of XPS peak areas enabled quantitative analysis of the WTe_2 surface. We found that the area ratio of W *4f* and Te *3d* peaks after vacuum-annealing decreased significantly from 1:2 to 1:0.6 (Table S1). Considering the fact that XPS measurement is sensitive to the surface, we speculate that the surface of WTe_2 has more Te vacancies than the bulk of WTe_2.

Even though the chemical state was modified by Te vacancies on the surface of WTe_2, the surface morphology remained almost unchanged. WTe_2 flakes were mechanically exfoliated on Si/SiO_2 substrates by the scotch tape method, and the flakes were studied by AFM before and after the *in-situ* vacuum-annealing process with a vacuum of 1×10^{-8} Torr. In Fig. 2c, the surface roughness of the pristine and annealed WTe_2 were 13.2 Å and 10.0 Å, respectively. However, the surface morphology changed dramatically on annealing at temperatures above 673 K probably due to the high Te deficiency (see Fig. S3). This indicates that a mild annealing process at temperatures less than 473 K preserves the pristine surface morphology with uniformly distributed Te vacancies on the flat WTe_2 surface.

To study the role of the Te vacancy in the electrochemical catalytic activity, HER performances of the pristine and vacuum-annealed WTe_2 single crystal were measured. Fig. 2d shows the voltammetry polarization curves of the pristine and vacuum-annealed WTe_2 single crystal. The overpotential obtained at a current density of 1.0 mA/cm^2 was –0.53 V and –0.40 V for pristine and Te-deficient WTe_2, respectively (inset in Fig. 2d), and the Tafel slopes in Fig. 2e obtained from polarization curves remained almost unchanged within a range between 154 and 159 mV/dec. Considering the large Tafel slope of 154 mV/dec in pristine and 159 mV/dec in vacuum-annealed WTe_2, the Te vacancies seemed to be too insignificant to increase the rate of hydrogen conversion at catalytic active sites.

A decrease in the overpotential with the unchanged Tafel slope could be explained by the change in the bulk transport properties in Te-deficient WTe_2. We acquired UPS spectra for the pristine and Te-deficient WTe_2 single crystal and estimated the work function from the secondary cut-off in the UPS spectra. A UPS spectrum was recorded after exfoliation in a vacuum chamber (base pressure: 1×10^{-10} Torr) with scotch tape for pristine WTe_2 and another was obtained after *in-situ* vacuum-annealing for Te-deficient WTe_2 (annealing conditions were the same as those for annealed WTe_2 for XPS measurements, results of which are shown in Fig. 2b). Pristine WTe_2 exhibited a work function of 4 eV while Te-deficient WTe_2 exhibited a work function of 3 eV. We found that the work function decreased for the Te-deficient WTe_2 surface by 1 eV (see Fig. 3a).

To support our experimental findings, first-principles density functional theory (DFT) calculations were performed to estimate the work function of WTe_2 without or with Te vacancies as seen in Fig. 3b. The thickness dependence of the calculated work function was rather strong in mono- and bilayers of WTe_2 and saturated at approximately 4.66 eV above three layers of WTe_2 (see Figs. S4, S5). Considering the bulky WTe_2 samples, we estimated the work function of the pristine WTe_2 as 4.66 eV. To obtain the work function of Te-deficient WTe_2, we considered two types of Te vacancies created at α sites and β sites with a

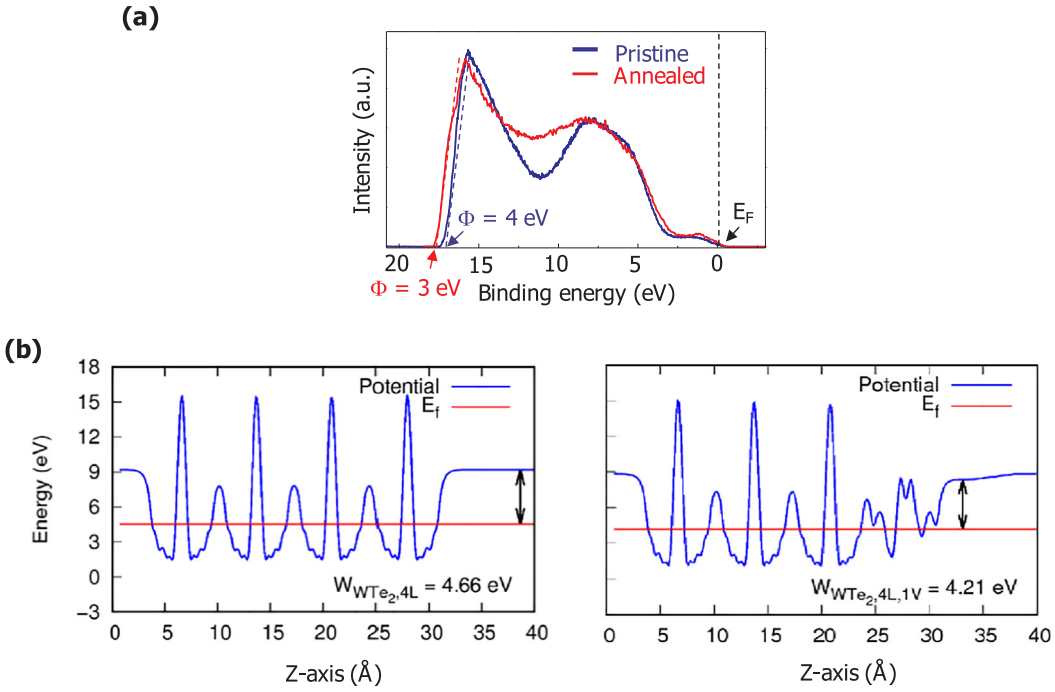

Fig. 3. (a) UV photoemission spectra before and after *in-situ* vacuum-annealing on WTe_2 single crystal. Secondary cut-off values show changes in the work functions (Φ) from 4 to 3 eV after vacuum-annealing process. (b) DFT calculations for work function of 4-layer WTe_2 with/without vacancies at α site (one Te vacancy in one unit cell).

concentration of 4.46×10^{14} cm^{-2} (single Te vacancy in one unit cell). We found that the work function of WTe_2 decreased down to 4.21 eV with α site Te vacancies, while the work function increased up to 4.75 eV with β site Te vacancies. The decreased work function with α site Te vacancies was consistent with our UPS analysis. Recently published papers have also reported the effective electron doping via chalcogen vacancy creation, which can lead to an upward shift in the Fermi level in metallic the group 6 TMDs [34,35].

High-temperature vacuum-annealing was used to produce Te vacancies with a high density at the WTe_2 surface. However, because the defective WTe_2 surface is easily and seriously oxidized in air when the sample is transfered to other analysis tools, we developed a new way of generating a highly Te-deficient WTe_2 surface and characterizing its *in-situ* HER performances: electrochemical reduction in an acidic solution using voltage cycling. In Fig. 4a, SEM images of WTe_2 obtained from samples with different CV cycles show that the surface morphology changed significantly up to 8000 CV cycles. The LSV curves of the samples in Fig. 4a are shown in Fig. S6. The electrochemical reduction produced a rough surface of WTe_2 due to dissolution of Te into the acidic solution ($WTe_2 \rightarrow WTe_{2-x} + xTe$), which was verified by the EDX and MS-ICP results of the electrolyte (see Fig. S7); accordingly, the electrochemically-reduced WTe_2 surface was largely modified by Te vacancies.

The highly-concentrated Te vacancies at the WTe_2 surface induced the diffusion of Te ions from the (inside) bulk to the (top) surface during the electrochemical reduction. As the CV cycling continued, the thickness of the Te-deficient area increased. We note that the capacity of Te ion diffusion from the insider area was limited. Therefore, we achieved saturated Te vacancies at the top surface of the WTe_2 after a certain number of CV cycles where creating vacancies was terminated. We estimate the thickness of the Te-deficient region from the top surface as less than a few tens of nanometers by comparing surface-sensitive XPS and bulk-sensitive x-ray diffraction (XRD) (see Fig. S8).

The chemical state of Te-deficient WTe_2 with a rough surface was studied using XPS measurements. As seen in Fig. 4b, W *4f* and Te *3d* spectra obtained after electrochemical reduction showed multiple features corresponding to WTe_2, WTe_{2-x}, and some oxides. The core levels of W *4f* and Te *3d* were located at 33.2 eV (W $4f_{7/2}$, red) and 574.1 eV (Te $3d_{5/3}$, red), respectively, with a Te/W ratio of 2 and a binding energy interval of 540.9 eV that was consistent with the results obtained for pristine WTe_2, as shown in Fig. 2b. We considered that the W *4f* and Te *3d* peaks at 34.6 eV and 573.46 eV were due to the Te-deficient WTe_2 because the ratio of W *4f* and Te *3d* peaks was almost 1:0.6. In addition, the binding energy interval between W *4f* and Te *3d* was 538.86 eV, which was smaller than that of pristine by 2.04 eV. Fitting results are summarized in Table S1.

To determine the effect of the surface morphology on the catalytic activity, HER performances of WTe_2 were determined for various CV cycles. Fig. 4c–e show largely enhanced electrocatalytic activity on the rough WTe_2 surface with an overall decrease in the overpotential from −0.707 to −0.119 V and in the Tafel slope from 154 to 79 mV/dec. After 8000 cycles, enhancement in the HER performance became saturated and stabilized with an overpotential of 0.119 V and Tafel slope of 79 mV/dec for the rough WTe_2 surface (SEM image shown in Fig. 4a).

To study the effects of the Te vacancy on the HER performance, we estimated the turnover frequency (TOF) for pristine WTe_2 and vacuum-annealed WTe_2 for hydrogen adsorption at the surface. Theoretical calculations predicted that Te sites in distorted metallic TMDs, α and β sites (Fig. 1a), exhibit different hydrogen adsorption energies (ΔE_H) of 0.64 eV (α sites) and 1.54 eV (β sites) (see Fig. S9). The most active Te atoms are located at the α sites with smallest Gibbs free energy, 1.14 eV (see Fig. S10). We assumed that Te atoms at β sites would still behave as active sites in vacuum-annealed WTe_2. The deduced TOF of vacuum-annealed WTe_2 was 0.064 s^{-1}, which was rather enhanced compared to that of pristine WTe_2, 0.014 s^{-1}, probably due to the enhanced bulk conductivity in vacuum-annealed WTe_2 (details are given in the supporting materials). We summarized the HER performances of pristine WTe_2, vacuum-annealed WTe_2, electrochemically-reduced WTe_2, metallic $MoTe_2$ (1T'), and bulk Pt for comparison in Table 1.

We further studied the changes of the HER active area in the electrochemically-reduced WTe_2 surface that had an increase of the surface

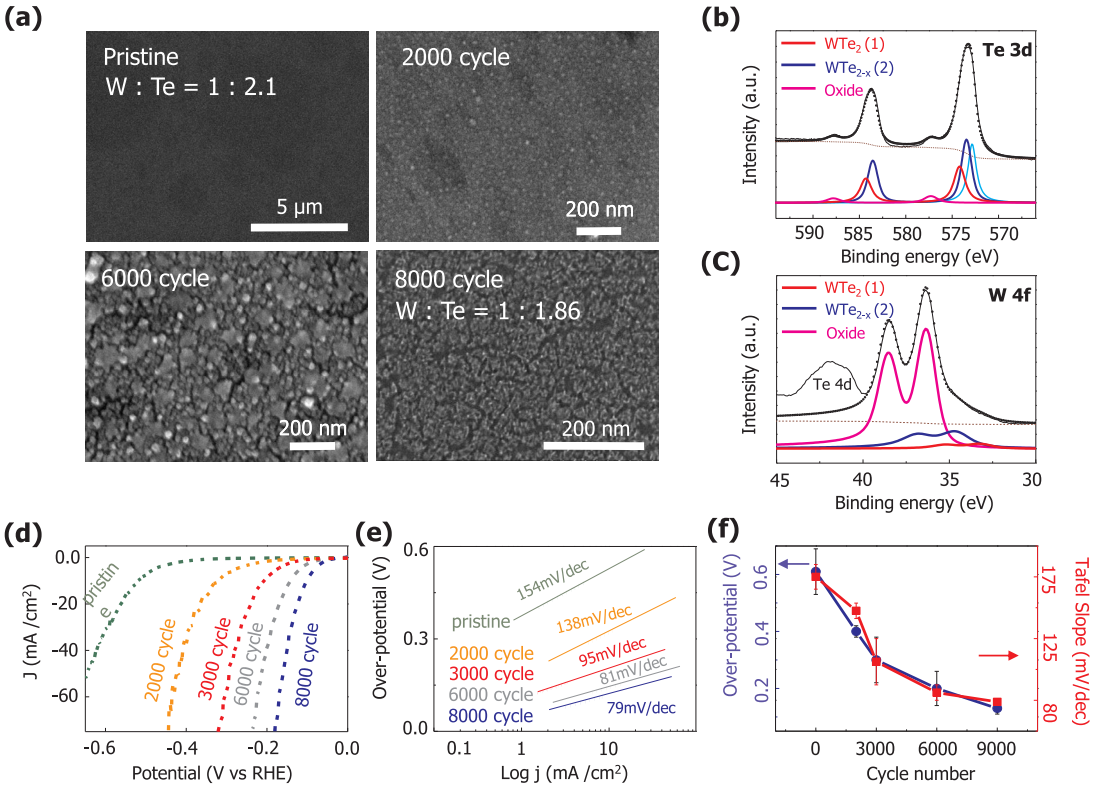

Fig. 4. (a) SEM images and Te/W ratio of the surface of pristine crystal, after 2000, 6000, and 8000 CV cycles. (LSV curve of each samples with different CV cycles are in Fig. S6) X-ray photoemission spectra of core levels, (b) W *4f*, and (c) Te *3d* obtained for electrochemically-reduced WTe_2 surface after 9000 CV cycles.The single peak with cyan color corresponds to peak of Ag $3p_{3/2}$. (d) Linear polarization curves and (e) Tafel plots of various CV cycles. (f) Comparison of the overpotential (at 10 mA/cm^2) and the Tafel slope for different cycle numbers of various CV cycles.

roughness. The electrochemical active surface area (ECSA) analysis was conducted with pristine and electrochemically-reduced WTe_2. Fig. 5a shows that the hysteresis of current density (J) varies with different scan rates (from 20 to 200 mV/s). We estimated the double layer capacitance (C_{dl}) from the slopes in the plots of the current density as a function of scan rate in Fig. 5b as 0.0257 and 6.1 mF/cm^2 for pristine and electrochemically-reduced WTe_2, respectively. We assumed that Te-deficient WTe_2 via vacuum-annealing and electrochemical reduction had similar TOF values of 0.064 s^{-1}, but the electrochemically-reduced WTe_2 had an enlarged ECSA due to a large increase in surface roughness, which led to a high HER performance with decreases in Tafel slopes and overpotentials.

4. Conclusion

The catalytic performance of hydrogen evolution was studied on metallic WTe_2 single-crystals and Te-deficient WTe_2 surfaces. We found that the Te vacancies enhanced the bulk conductivity of WTe_2 with a decreased work function. The surface morphology was highly modified by Te vacancies, resulting in an increase in the electrochemical active surface area. We suggest that the increase in bulk conductivity and the electrochemical active surface area in Te-deficient WTe_2 could be the main reasons for recently reported excellent HER performances of metallic transition metal dichalcogenides with chalcogen vacancies. Our study clarifies the role of chalcogen vacancies for the electrocatalytic activity and paves the way to find a new strategy for designing an ideal electrochemical catalyst using metallic layered materials.

CRediT authorship contribution statement

Hagyeong Kwon: Data curation, Investigation, Writing - original draft, Writing - review & editing. **Byungdo Ji:** Data curation, Investigation, Writing - original draft. **Dongyeon Bae:** Data curation, Investigation. **Jun-Ho Lee:** Formal analysis. **Hee Jung Park:** Investigation. **Do Hyun Kim:** Investigation. **Young-Min Kim:** Investigation. **Young-Woo Son:** Formal analysis. **Heejun Yang:** Conceptualization, Supervision. **Suyeon Cho:** Conceptualization, Supervision, Writing - original draft, Writing - review & editing.

Declaration of Competing Interest

The authors declare that they have no known competing financial

Table 1
Comparison of catalytic activities of pristine, vacuum-annealed WTe_2 and electrochemically-reduced WTe_2 together with two references, metallic 1T'-$MoTe_2$ and bulk platinum film adopted from reference [24].

Catalyst	Potential for 10 mA/cm^2 (V versus RHE)	Tafel slope (mV per decade)	Exchange current density (mA/cm^2)	TOF (s^{-1})
Pristine WTe_2	−0.707	154	2.0×10^{-3}	0.014
Vacuum-annealed WTe_2	−0.568	159	9.4×10^{-3}	0.064
Electrochemically-reduced WTe_2	−0.119	79	3.0×10^{-1}	–
1T'-$MoTe_2$ [24]	−0.356	127	2.1×10^{-2}	0.14
Pt [24]	−0.046	36	4.5×10^{-1}	0.94

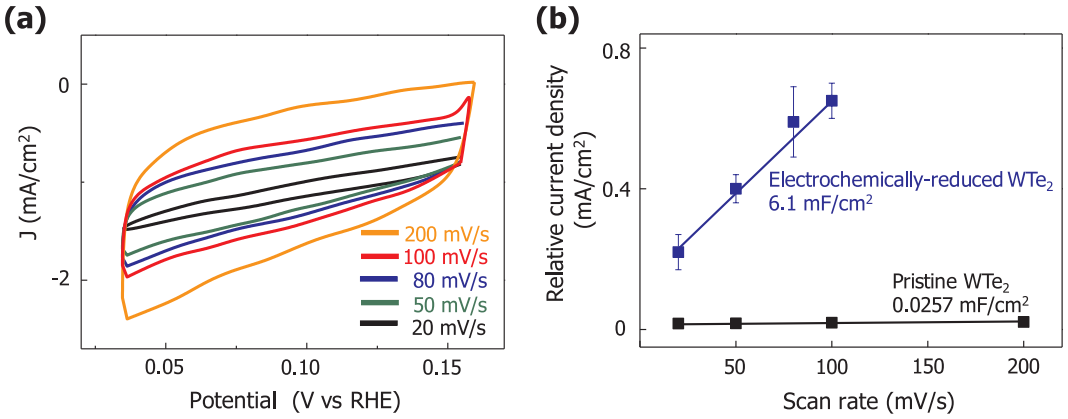

Fig. 5. Electrochemical active surface area (ECSA) analysis (a) Cyclic Voltammetry curves of the electrochemically-reduced WTe_2 measured in a non-faradic region from 0.035 to 0.16 V vs. RHE with various scan rates of 20, 50, 80,100 and 200 mV/s (b) Double layer capacitance (C_{dl}) of the pristine (black) and the electrochemically-reduced WTe_2 (blue line), respectively. (For interpretation of the references to colour in this figure legend, the reader is referred to the web version of this article.)

interests or personal relationships that could have appeared to influence the work reported in this paper.

Acknowledgements

This work was supported by the Ewha Womans University Research Grant of 2017. S.C., H.K. and D.B. were supported by the Basic Science Research Program through the National Research Foundation of Korea (NRF) funded by the Ministry of Science, ICT and Future Planning (2020R1A2C2003377). H.Y. acknowledges support from the National Research Foundation of Korea (NRF) under Grant No. NRF-2020R1A2B5B02002548. Y.-W.S. was supported by the NRF of Korea (Grant No. 2017R1A5A1014862, SRC program: vdWMRC Center). We thank the Korea Institute for Advanced Study for providing computing resources (KIAS Center for Advanced Computation Linux Cluster System) for this work. Y.-M.K. acknowledges financial support from the Institute for Basic Science (IBS-R011-D1).

Appendix A. Supplementary material

Supplementary data to this article can be found online at https://doi.org/10.1016/j.apsusc.2020.145972.

References

[1] Y. Tachibana, L. Vayssieres, J.R. Durrant, Artificial photosynthesis for solar water-splitting, Nat. Photon. 6 (2012) 511–518.
[2] G.A. Olah, Towards oil independence through renewable methanol chemistry, Angew. Chem., Int. Ed. 52 (2013) 104–107.
[3] X. Zou, Y. Zhang, Noble metal-free hydrogen evolution catalysts for water splitting, Chem. Soc. Rev. 44 (2015) 5148–5180.
[4] Y.A. Lyon, A.A. Roberts, D.R. McMillin, Exploring hydrogen evolution and the overpotential, J. Chem. Educ. 92 (2015) 2130–2133.
[5] C.S. Lim, S.M. Tan, Z. Sofer, M. Pumera, Impact electrochemistry of layered transition metal dichalcogenides, ACS Nano. 9 (2015) 8474–8483.
[6] M. Lozada-Hidalgo, et al., Sieving hydrogen isotopes through two-dimensional crystals, Science 351 (2016) 68–70.
[7] M. Chhowalla, et al., The chemistry of two-dimensional layered transition metal dichalcogenide nanosheets, Nat. Chem. 5 (2013) 263–275.
[8] Z. Gholamvand, et al., Comparison of liquid exfoliated transition metal dichalcogenides reveals $MoSe_2$ to be the most effective hydrogen evolution catalyst, Nanoscale 8 (2016) 5737–5749.
[9] H. Li, et al., Activating and optimizing MoS_2 basal planes for hydrogen evolution through the formation of strained sulphur vacancies, Nat. Mater. 15 (2016) 48–53.
[10] T.F. Jaramillo, et al., Identification of active edge sites for electrochemical H_2 evolution from MoS_2 nanocatalysts, Science 317 (2007) 100–102.
[11] X. Long, et al., Metallic iron-nickel sulfide ultrathin nanosheets as a highly active electrocatalyst for hydrogen evolution reaction in acidic media, J. Am. Chem. Soc. 137 (2015) 1900–11903.
[12] D. Voiry, et al., The role of electronic coupling between substrate and 2D MoS_2 nanosheets in electrocatalytic production of hydrogen, Nat. Mater. 15 (2016) 1003–1009.
[13] S.S. Chou, et al., Understanding catalysis in a multiphasic two-dimensional transition metal dichalcogenide, Nat. Commun. 6 (2015) 8311.
[14] R. Subbaraman, et al., Enhancing hydrogen evolution activity in water splitting by tailoring Li^+-$Ni(OH)_2$-Pt interfaces, Science 334 (2011) 1256–1260.
[15] D.K. Biegelsen, R.A. Street, C.C. Tsai, J.C. Knights, Hydrogen evolution and defect creation in amorphous Si: H alloys, Phys. Rev. B 20 (1979) 4839.
[16] D. Kiriya, et al., General thermal texturization process of MoS_2 for efficient electrocatalytic hydrogen evolution reaction, Nano Lett. 16 (2016) 4047–4053.
[17] G. Ye, et al., Defects engineered monolayer MoS_2 for improved hydrogen evolution reaction, Nano Lett. 16 (2016) 1097–1103.
[18] C.G. Morales-Guio, L.A. Stern, X. Hu, Nanostructured hydrotreating catalysts for electrochemical hydrogen evolution, Chem. Soc. Rev. 43 (2014) 6555–6569.
[19] N.H. Attanayake, et al., Effect of intercalated metals on the electrocatalytic activity of 1T- MoS_2 for the hydrogen evolution reaction, ACS Energy Lett. 3 (2017) 7–13.
[20] P.D. Tran, et al., Coordination polymer structure and revisited hydrogen evolution catalytic mechanism for amorphous molybdenum sulfide, Nat. Mater. 15 (2016) 640–646.
[21] S. Lee, et al., Origin of extremely large magnetoresistance in the candidate type-II Weyl semimetal $MoTe_{2-x}$, Sci. Rep. 8 (2018) 13937.
[22] S. Cho, et al., Phase patterning for ohmic homojunction contact in $MoTe_2$, Science 349 (2015) 625–628.
[23] H. Yang, S.W. Kim, M. Chhowalla, Y.H. Lee, Structural and quantum-state phase transitions in van der Waals layered materials, Nat. Phys. 13 (2017) 931–937.
[24] J. Seok, et al., Active hydrogen evolution through lattice distortion in metallic $MoTe_2$, 2D Mater 4 (2017) 025061.
[25] Y.A. Eshete, et al., Vertical heteropha+se for electrical, electrochemical, and mechanical manipulations of layered $MoTe_2$, Adv. Funct. Mater. 29 (2019) 1904504.
[26] J. Seok, et al., Hybrid catalyst with monoclinic $MoTe_2$ and platinum for efficient hydrogen evolution, APL Mater. 7 (2019) 071118.
[27] N. Ling, et al., In-operando stacking of reduced graphene oxide for active hydrogen evolution, ACS Appl. Mater. Interf. 11 (2019) 43460–43465.
[28] J. Lee, et al., Hydrogen evolution reaction at anion vacancy of two-dimensional transition-metal dichalcogenides: Ab initio computational screening, J. Phys. Chem. Lett. 9 (2018) 2049–2055.
[29] C. Wei, et al., Atomic plane-vacancy engineering of transition-metal dichalcogenides with enhanced hydrogen evolution capability, ACS Appl. Mater. Interf. 11 (2019) 25264–25270.
[30] D.H. Keum, et al., Bandgap opening in few-layered monoclinic $MoTe_2$, Nat. Phys. 11 (2015) 482–486.
[31] P. Giannozzi, et al., QUANTUM ESPRESSO a modular and open-source software project for quantum simulations of materials, J. Phys.: Condens. Matter. 21 (2009) 395502.
[32] J.P. Perdew, K. Burke, M. Ernzerhof, Generalized gradient approximation made simple, Phys. Rev. Lett. 77 (1996) 3865–3868.
[33] Y. Kim, et al., Anomalous Raman scattering and lattice dynamics in mono- and few-layer WTe_2, Nanoscale 8 (2016) 2309–2316.
[34] S.H. Kang, et al., Superconductivity in Te-deficient polymorphic MoTe2-x and its derivatives: rich structural and electronic phase transitions, 2D Mater. 5 (2018) 031014.
[35] S. Cho, et al., Te vacancy-driven superconductivity in orthorhombic molybdenum ditelluride, 2D Mater. 4 (2017) 021030.